J. Fluid Mech. (1993), *vol.* 250, *pp.* 209–232

Convection in a rotating spherical fluid shell with an inhomogeneous temperature boundary condition at infinite Prandtl number

By KEKE ZHANG† AND DAVID GUBBINS
Department of Earth Sciences, University of Leeds, Leeds, LS2 9JT, UK

(Received 21 November 1991 and in revised form 16 October 1992)

We examine thermal convection in a rotating spherical shell with a spatially non-uniformly heated outer surface, concentrating on three distinct heating modes: first, with wavelength and symmetry corresponding to the most unstable mode of the uniformly heated problem; secondly, with the critical wavelength but opposite equatorial symmetry; and thirdly, with wavelength much larger than that of the most unstable mode. Analysis is focused on boundary-locked convection, the associated spatial resonance phenomena, the stability properties of the resonance solution, and time-dependent secondary convection. A number of new forms of instability and convection are found: the most interesting is perhaps the saddle-node bifurcation, which is the first to be found for realistic fluid systems governed by partial differential equations. An analogous Landau amplitude equation is also analysed, providing an important mathematical framework for understanding the complicated numerical solutions.

1. Introduction

There are a number of fundamental issues central to the application of an ideal model of rotating spherical convection to real geophysical systems. One of them, which is of vital concern to geophysicists, is the likely effect of imperfections at the core–mantle boundary on convection in the Earth's core and on the magnetic field, whether the imperfections be in topography (Hide 1967), heat flux (Bloxham & Gubbins 1985), or material properties. Gubbins & Richards (1986) proposed a correlation between the main features of the geomagnetic field at the core–mantle boundary and temperature anomalies in the lower mantle, with the geodynamo controlled by prominent features of the lower mantle (Gubbins & Bloxham 1987). We have therefore set up an idealized problem in order to understand the possible thermal coupling between the core and the mantle. In an earlier paper (Zhang & Gubbins 1992) we explored flows driven by an imposed, laterally varying, boundary temperature and in this paper we examine the effect of such a boundary condition on convective instability. We refer to convection with an ideal homogeneous boundary condition as the uniform boundary problem, and convection with an inhomogeneous boundary condition as the non-uniform boundary problem.

The timescale of mantle convection is much longer than that of core convection and therefore the thermal effect of the mantle on the core can be simulated by assuming a stationary non-uniform boundary condition for core convection. We thus consider the problem of classical thermal convection in a rotating spherical fluid shell

† Present address: Department of Mathematics, University of Exeter, Exeter, EX4 4QJ, UK.

(Chandrasekhar 1961), but with a non-uniform temperature boundary condition on the outer spherical surface. The problem is governed by the Taylor number, T, measuring the rate of rotation, the Rayleigh number, R, associated with the strength of convective instability, and an imperfection parameter, ϵ, defined as the ratio of the typical temperature difference on the outer surface to the temperature difference across the fluid shell. In addition, the scale and symmetry of the non-uniform boundary are of crucial importance. It is not feasible to explore fully the parameter space of the problem; fortunately the system exhibits a smooth dependence on the Taylor number at infinite Prandtl number (Zhang & Busse 1990) and we therefore concentrate on two representative Taylor numbers, $T = 10^4$ and 10^5, for which Coriolis forces are strong but not so large as to make nonlinear solutions difficult to compute.

Though our main motivation is concerned with understanding the geophysical phenomenon, the problem is also of great interest to rotating fluid mechanics in general. In a rotating spherical fluid system there exist two types of basic flows: convective and baroclinic. Convective flows resulting from an instability of the basic state are in most cases driven by a radial temperature gradient across a spherical shell, the simplest case being a uniform distribution of heat sources (Chandrasekhar 1961). Baroclinic flows may be maintained by an externally imposed temperature variation on the boundary (e.g. Zhang & Gubbins 1992). In realistic systems, these two flows are likely to occur at the same time. As a result of the non-uniform temperature boundary condition, there exists, in contrast to the uniform boundary problem, no static equilibrium, and the unperturbated state is a steady flow, which is referred to as forced convection in this paper.

The non-uniform boundary problem of spherical rotating convection differs in a fundamental way from the non-uniform boundary problem of Rayleigh–Bénard convection (Kelly & Pal 1976, 1978; Weber 1973): the natural mode of rotating spherical convection for the uniform boundary problem is a travelling thermal Rossby wave. Kelly & Pal (1976, 1978) investigated Rayleigh–Bénard convection, subject to a spatially periodic horizontal boundary temperature at small amplitude near the onset of convection. Their studies were restricted to a non-uniformly heated boundary at onset of convection. They found that the amplitude of convection could be considerably enhanced in the neighbourhood of the critical Rayleigh number of the uniform boundary problem. The regime of higher Rayleigh numbers was investigated by Yoo & Kim (1991), revealing more complicated time-dependent behaviour of the two-dimensional convection. No similar studies have been conducted in a system with rotation and spherical geometry. However, the combination of rotation and spherical geometry markedly changes the dynamical behaviour of the non-uniform boundary problem in a rotating spherical fluid shell. The convective flows are in the form of thermal Rossby waves (e.g. Busse 1983) which attempt to pass over the non-uniform boundary; the baroclinic flows produced by the spatial variation on the boundary, on the other hand, are likely to be locked into the boundary for a large range of parameters (Zhang & Gubbins 1992). These distinct features bring a wealth of new dynamics to the non-uniform boundary problem of spherical rotating convection and may have significant implications in the geophysical context.

In a very general context, the bifurcation problem with spatially periodic external forcing has been studied on the basis of the amplitude equation approach (e.g. Coullet, Repaux & Vanel 1986; Coullet & Repaux 1987). Emphasis is on the effects of the difference between an external forcing wavelength and natural preferred wavelength. It was shown that the pattern is locked if the scale of the external forcing is close enough to the preferred natural scale, but transitions to quasi-periodic patterns occur if the gap

between the natural and the external wavelength is increased. While the full nonlinear numerical approach involving partial differential equations reveals detailed physical phenomena, a model system with an ordinary differential equation usually provides deep insight into the mathematical structure of the problem. One such system is the analogous Landau amplitude equation

$$\dot{A} = (\mu + \mathrm{i}\omega) A - A|A|^2 + \epsilon,$$

where A is a complex variable, μ, ϵ are small real parameters, and ω is a real constant. The parameter μ is similar to the supercritical Rayleigh number; ϵ resembles the small imperfection parameter above which is also denoted by ϵ; and ω is related to the Taylor number determining the frequency of oscillation for the uniform boundary problem $\epsilon = 0$. The relevant aspects of this amplitude equation, being parallel to our nonlinear numerical analysis of the spherical rotating convection, are studied in the Appendix, which provides an important mathematical framework in the discussion and understanding of the numerical results.

The primary objective of the present paper is to examine how slight deviations from an idealized temperature boundary condition can influence convection in a rotating spherical fluid shell in the limit of infinite Prandtl number. The forced convection, linear stability of the forced convection and the subsequent nonlinear evolution of the non-uniform boundary problem are investigated. The paper will concentrate on the effects of different strengths, scales and symmetries of the temperature boundary imperfection. Three distinct classes of the spatial variation of the outer boundary condition are investigated: (i) the wavelength and equatorial symmetry of the boundary condition are the same as those of the most unstable mode of the uniform boundary problem; (ii) the boundary condition has the same wavelength as that of the most unstable mode but antisymmetry with respect to the equatorial plane; (iii) the scale of the boundary temperature variation is substantially different from the critical wavelength. The most interesting region of parameter space lies near the critical Rayleigh number of the uniform boundary problem, where spatial resonance phenomena of the non-uniform boundary problem can occur.

The mathematical equations are set up in §2; different forms of the forced convection and the spatial resonance phenomenon are discussed in §3; the stability properties of the forced convection are shown in §4; secondary convection, with a variety of time-dependences, including the saddle-node bifurcation, is presented in §5; and closing remarks are made in §6.

2. Mathematical formulation of the problem

2.1. *Basic equations*

As the basic equations are similar to those described in Zhang (1991) (hereafter referred to as Z1), this section is kept brief. Consider a rotating spherical fluid shell of constant thermal diffusivity, κ, constant coefficient of thermal expansion, α, and constant viscosity, ν, with a uniform distribution of heat sources which produce the basic temperature gradient, $\nabla T_s = -\beta r$. Using $d = r_o - r_i$, d^2/κ, $d^2\beta$ as scales for length, time and temperature, respectively, fluid motions at infinite Prandtl number are governed by the following nonlinear equations:

$$(\nabla^2 \mathscr{L}_2 + T^{\frac{1}{2}} \partial/\partial\phi)\, \nabla^2 v + T^{\frac{1}{2}} \mathscr{Q} w - R \mathscr{L}_2 \Theta_1 = 0, \tag{1}$$

$$(\nabla^2 \mathscr{L}_2 + T^{\frac{1}{2}} \partial/\partial\phi)\, w - T^{\frac{1}{2}} \mathscr{Q} v = 0, \tag{2}$$

$$(\nabla^2 - \partial/\partial t)\, \Theta_1 + \mathscr{L}_2 v = \boldsymbol{u} \cdot \nabla \Theta_1, \tag{3}$$

where the temperature deviation from the pure conducting state is denoted by Θ_1, the differential operators $\mathscr{Q}$ and $\mathscr{L}_2$, are the same as defined in Z1, and the velocity $\boldsymbol{u}$ is expressed as a sum of poloidal and toroidal vectors

$$\boldsymbol{u} = \nabla \times \nabla \times r v + \nabla \times r w.$$

The physical parameters of the problem, the Rayleigh number, R, the Prandtl number, Pr, and the Taylor number, T, are defined as

$$R = \frac{\alpha \beta \gamma d^6}{\nu \kappa}, \quad Pr = \frac{\nu}{\kappa}, \quad T = \left(\frac{2\Omega d^2}{\nu}\right)^2.$$

At infinite Pr the only nonlinearity is the advection term in (3). The velocity boundary conditions are obtained by assuming impenetrable, stress-free boundaries at the inner and outer surfaces of the shell,

$$v = \frac{\partial^2 v}{\partial r^2} = \frac{\partial}{\partial r}\left(\frac{w}{r}\right) = 0. \tag{4}$$

A perfect thermal-conducting boundary is assumed at the inner spherical surface while the temperature at the outer boundary is prescribed:

$$\Theta_1 = 0, \quad r = r_i; \quad \Theta_1 = \epsilon \Theta_s(\theta, \phi), \quad r = r_o \tag{5}$$

where ϵ is an 'imperfection parameter' defined as

$$\epsilon = \mathscr{T}/\beta d^2,$$

and $\mathscr{T}$ is the typical amplitude of the boundary temperature variation.

The non-uniform boundary problem of convection defined by (1)–(3) and boundary conditions (4)–(5) is solved in three stages. First, steady three-dimensional solutions are obtained in terms of the parameter T, R, ϵ and different patterns and symmetries of Θ_s. Secondly, stability of the nonlinear steady solutions is analysed with general infinitesimal three-dimensional perturbations. Finally, bifurcation solutions of the system are obtained for the parameter region where at least one such disturbance grows with time.

2.2. *Forced (steady) convection*

A rotating spherical system subject to a non-uniform temperature boundary condition cannot have a static conducting state, $\boldsymbol{u} = 0$, for a finite value of ϵ. In the presence of a non-uniformly heated boundary, a baroclinic flow is produced and a mean flow can also be generated. Generally speaking, the nonlinear equations must be solved to find a steady solution of the system. While the expansions for the velocity field are the same as in Z1 we expand the temperature as

$$\Theta_1 = \epsilon f(r)\, \Theta_s + \Theta,$$

where the function

$$f(r) = \sin\left[\frac{\pi(r - r_i)}{2(r_o - r_i)}\right]$$

is chosen with $f(r_i) = 0$ and $f(r_o) = 1$ so as to make the boundary conditions on Θ, the unknown temperature, homogeneous:

$$\Theta(r_i, \theta, \phi) = \Theta(r_o, \theta, \phi) = 0. \tag{6}$$

The governing nonlinear equations thus become inhomogeneous:

$$(\nabla^2 \mathscr{L}_2 + T^{\frac{1}{2}} \partial/\partial\phi)\, \nabla^2 v + T^{\frac{1}{2}} \mathscr{Q} w - R \mathscr{L}_2 \Theta = \epsilon R f(r)\, \mathscr{L}_2 \Theta_s \tag{7}$$

$$(\nabla^2 \mathscr{L}_2 + T^{\frac{1}{2}} \partial/\partial\phi)\, w - T^{\frac{1}{2}} \mathscr{Q} v = 0 \tag{8}$$

$$\nabla^2 \Theta + \mathscr{L}_2 v - \boldsymbol{u} \cdot \nabla \Theta = \epsilon (\boldsymbol{u} \cdot \nabla - \nabla^2) f(r)\, \Theta_s. \tag{9}$$

The expansion then used for the temperature Θ is the same as in the uniform boundary problem,

$$\Theta = \sum_{l,m,n} \Theta_{lmn} \sin n\pi(r-r_i)\, Y_l^m(\theta,\phi) + \text{c.c.},$$

where c.c. denote complex conjugate, the $Y_l^m(\theta,\phi)$ being normalized such that the spherical surface integral

$$\frac{1}{4\pi}\int_S |Y_l^m(\theta,\phi)|^2 \sin\theta \,\mathrm{d}\theta\,\mathrm{d}\phi = 1.$$

The problem becomes identical with the uniform boundary problem when $\epsilon = 0$, but it is important to note that the case $\epsilon = 0$ is fundamentally different from the case of $\epsilon \to 0$: the non-uniform boundary problem is essentially nonlinear because of the singularity at the onset of convection of the uniform boundary problem. The method of solution and truncation scheme are similar to those described in Z1.

2.3. *Instability analysis*

To investigate the stability of the steady solutions, denoted by (v_0, w_0, Θ_0), infinitesimal three-dimensional general perturbations, such as

$$\tilde{\Theta} = \sum_{l,m,n} \tilde{\Theta}_{lmn} \sin n\pi(r-r_i)\, Y_l^m(\theta,\phi) \exp(\mathrm{i}M\phi + \sigma t),$$

are superimposed onto the steady solution, where $\exp(\mathrm{i}M\phi)$ is the Floquet factor and the parameter M is an integer. The disturbances satisfy the same boundary conditions as the steady solution (v_0, w_0, Θ_0) and therefore the same expansions and truncation levels can be used. Substituting

$$(v, w, \Theta) = (v_0 + \tilde{v}, w_0 + \tilde{w}, \Theta_0 + \tilde{\Theta})$$

into (1)–(3), we can obtain the following linear homogeneous equations describing the stability of steady convection

$$(\nabla^2 \mathscr{L}_2 + T^{\frac{1}{2}}\partial/\partial\phi)\nabla^2\tilde{v} + T^{\frac{1}{2}}\mathscr{Q}\tilde{w} - R\mathscr{L}_2\tilde{\Theta} = 0, \tag{10}$$

$$(\nabla^2 \mathscr{L}_2 + T^{\frac{1}{2}}\partial/\partial\phi)\tilde{w} - T^{\frac{1}{2}}\mathscr{Q}\tilde{v} = 0, \tag{11}$$

$$(\nabla^2 - \sigma)\tilde{\Theta} + \mathscr{L}_2\tilde{v} - \boldsymbol{u}\cdot\nabla\tilde{\Theta} - \tilde{\boldsymbol{u}}\cdot\nabla\Theta_0 = \epsilon\tilde{\boldsymbol{u}}\cdot\nabla(f(r)\,\Theta_s). \tag{12}$$

This forms an eigenvalue problem with eigenvalue $\sigma = \sigma_r + i\sigma_i$, the real part of which represents the growth or decay rate of the perturbation, but only the eigenvalues which eventually control instability are of interest.

2.4. *Secondary convection*

If σ_i is finite at the instability boundary the secondary solution may be obtained by time-integration of the full nonlinear equations, but the absence of $\partial/\partial t$ terms in (1)–(2) means that a very costly implicit scheme must be used. Coefficients of the expansions of the three dependent variables thus become a function of time, for instance

$$\Theta = \sum_{l,m,n} \Theta_{lmn}(t) \sin n\pi(r-r_i)\, Y_l^m(\theta,\phi) + \text{c.c.}$$

With an implicit Crank–Nicolson-type scheme, the evolution of the system beyond the stability boundary is governed by the following equations between (v_i, w_i, Θ_i) at time t_i and $(v_{i+1}, w_{i+1}, \Theta_{i+1})$ at time $t_i + \Delta t$:

$$(\nabla^2 \mathscr{L}_2 + T^{\frac{1}{2}}\partial/\partial\phi)\nabla^2 v_{i+1} + T^{\frac{1}{2}}\mathscr{Q}w_{i+1} - R\mathscr{L}_2\Theta_{i+1} = \epsilon(R(f(r)\,\mathscr{L}_2\Theta_s), \tag{13}$$

$$(\nabla^2 \mathscr{L}_2 + T^{\frac{1}{2}}\partial/\partial\phi)w_{i+1} - T^{\frac{1}{2}}\mathscr{Q}v_{i+1} = 0, \tag{14}$$

$$\nabla^2(\Theta_{i+1} + \Theta_i) + \mathscr{L}_2(v_i + v_{i+1}) + N_{i,i+1} - 2(\Theta_{i+1} - \Theta_i)/\Delta t = \epsilon[(\boldsymbol{u}_i + \boldsymbol{u}_{i+1})\cdot\nabla - \nabla^2]f(r)\,\Theta_s, \tag{15}$$

where $N_{i,i+1} = -0.5[\boldsymbol{u}_i \cdot \nabla\Theta_i + \boldsymbol{u}_{i+1} \cdot \nabla\Theta_{i+1} + \boldsymbol{u}_i \cdot \nabla\Theta_{i+1} + \boldsymbol{u}_{i+1} \cdot \nabla\Theta_i]$.

The time-step, Δt, for the numerical integration is kept small enough to ensure accuracy and, for several cases, solutions are checked using different values of the time-step Δt.

3. Forced (steady) convection

3.1. *Boundary-resonant convection*

When the wavenumber and symmetry of the boundary condition are the same as the natural wavenumber and symmetry, spatial resonance is likely to occur, and the corresponding convection here is referred to as boundary resonant convection. Before proceeding to discussions of the results, it is appropriate first to introduce three important values of the Rayleigh number: R_c, the classical critical Rayleigh number for the onset of convection without imposing the non-uniform boundary to the system; R_{ic}, the Rayleigh number at which the forced steady solution becomes unstable and a bifurcation occurs, and the resonance Rayleigh number, R_r, at which the amplitude of convection reaches its peak.

In the neighbourhood of R_c, where the spatial resonance phenomenon is likely to take place, the nonlinearity of the system is the most crucial factor in determining the basic properties of the convection even if the imperfection parameter ϵ is infinitesimally small. Figure 1(*a*) shows the average kinetic energy, E, normalized by its maximum value, as a function of Rayleigh number for several values of ϵ with the boundary heating mode described by

$$\Theta_s(6,6) = (1+\mathrm{i})\, Y_6^6(\theta,\phi) + \text{c.c.} \tag{16}$$

at $T = 10^5$, where the critical wavenumber for the onset of convection is $m_c = 6$. Examples of the related structure of the convection are displayed in figure 1(*b–d*). For the purpose of comparison with the uniform boundary problem, it is worth mentioning that the forced convection is stationary and eventually locked into the boundary temperature anomalies; we shall sometimes refer this type of convection as 'boundary-locked'. The effects of the boundary anomalies in the neighbourhood of $(R-R_c)/R_c \ll 1$ are greatly amplified. This strong amplification is likely to be connected with the fact that the inertial term in the equation of motion ((1) and (2)) is neglected in the limit of large Prandtl number, even though the forced steady mode, with the natural wavenumber and symmetry, is not the natural mode of the whole system. As R approaches the critical region for the uniform boundary problem, the amplitude of convection increases sharply as a result of the spatial resonance. With $\epsilon \to 0$, we expect that $R_r \to R_c$, as observed in the non-uniform boundary problem of Rayleigh–Bénard convection (Kelly & Pal 1978). However, the resonance Rayleigh number R_r is strongly dependent on the imperfection parameter ϵ, which increases from about $R_r = 5500$ at $\epsilon = 0.01$ to about $R_r = 6200$ at $\epsilon = 0.025$. This is largely because spatial resonance is a nonlinear phenomenon and related to the amplitude of convection as determined primarily by the size of ϵ in the neighbourhood of R_c. With increasing $R-R_r$, the amplitude of convection decreases rapidly, usually indicating instability of the resonance solutions. For $R/R_c \ll 1$, the forced convection represents a flow driven mainly by the temperature anomalies on the boundary. This type of flow can exist even in a strongly stratified fluid $R < 0$ (Zhang & Gubbins 1992). A prograde phase shift of the convection rolls with respect to the temperature anomalies on the boundary is clearly noticeable with increasing R. At the peak amplitude of the

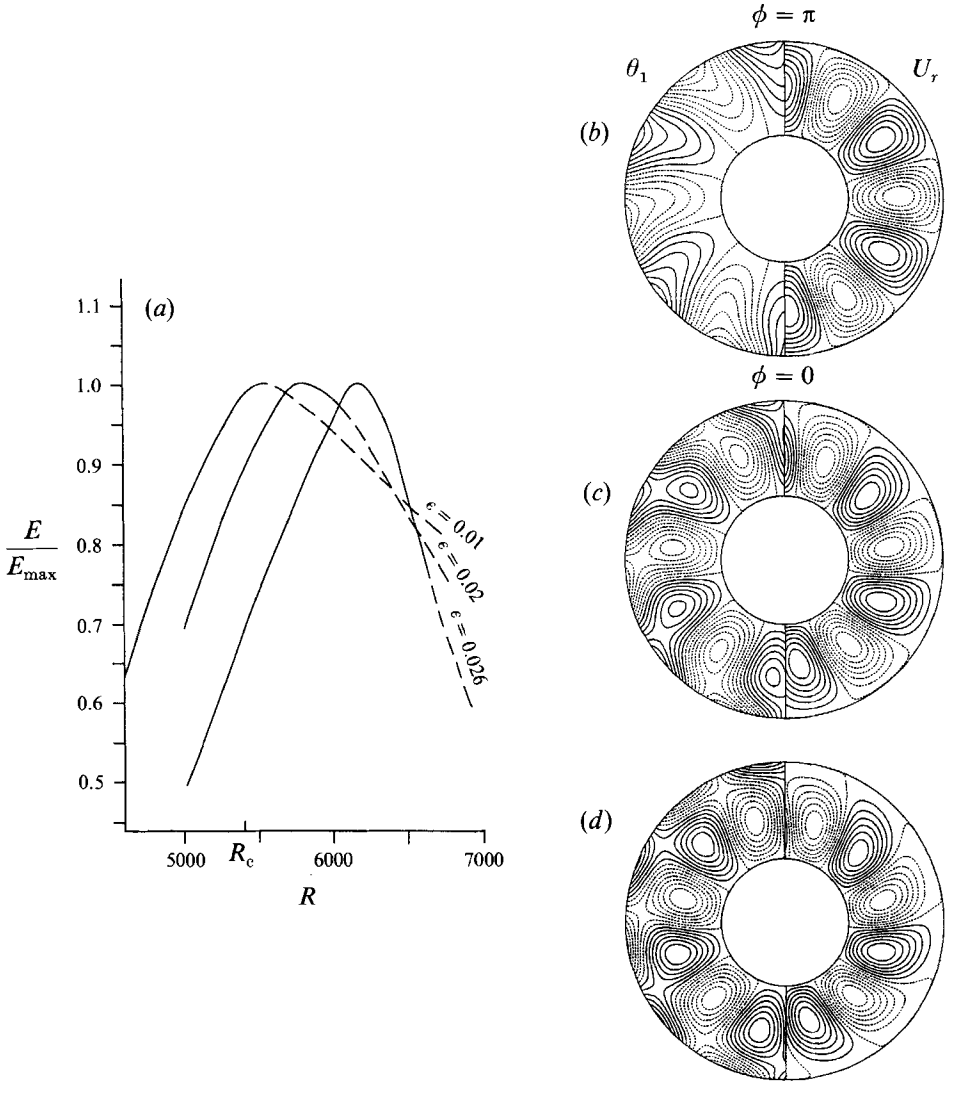

FIGURE 1. (*a*) Kinetic energies of boundary-resonance convection as a function of the Rayleigh number at different imperfection parameters ϵ for $\Theta_s(6,6)$ at $T = 10^5$. The $E_{\max}$ are 0.96, 4.85 and 10.8, corresponding to $\epsilon = 0.01$, 0.02 and 0.025, respectively. Dashed lines indicate unstable solutions. (*b–d*) Contours of Θ_1 (on the left-hand side) and contours of u_r (on the right-hand side) at the equatorial plane for (*b*) $R = 3000$, (*c*) $R = 4600$ and (*d*) $R = 5600$ at $T = 10^5$ and $\epsilon = 0.01$. The solid contours show $u_r > 0$; the dashed contours show $u_r < 0$ or $\Theta_1 < 0$.

resonance, $R \approx R_r$, the phase of the rolls is shifted about 180°, resulting in two temperature layers. This is clearly shown in figure 1(*d*). The instability analysis presented in the next section shows that this type of steady solution becomes unstable.

The larger the scale of the boundary anomalies the deeper its effects penetrate (Zhang & Gubbins 1992). We therefore expect that the effects of the imperfection would be dynamically more substantial if the scale of Θ_s were large enough to penetrate to a substantial depth. Figure 2 illustrates the effects of the scale on the non-uniform boundary problem for the case

$$\Theta_s(4,4) = (1+\mathrm{i})\, Y_4^4(\theta,\phi) + \text{c.c.} \tag{17}$$

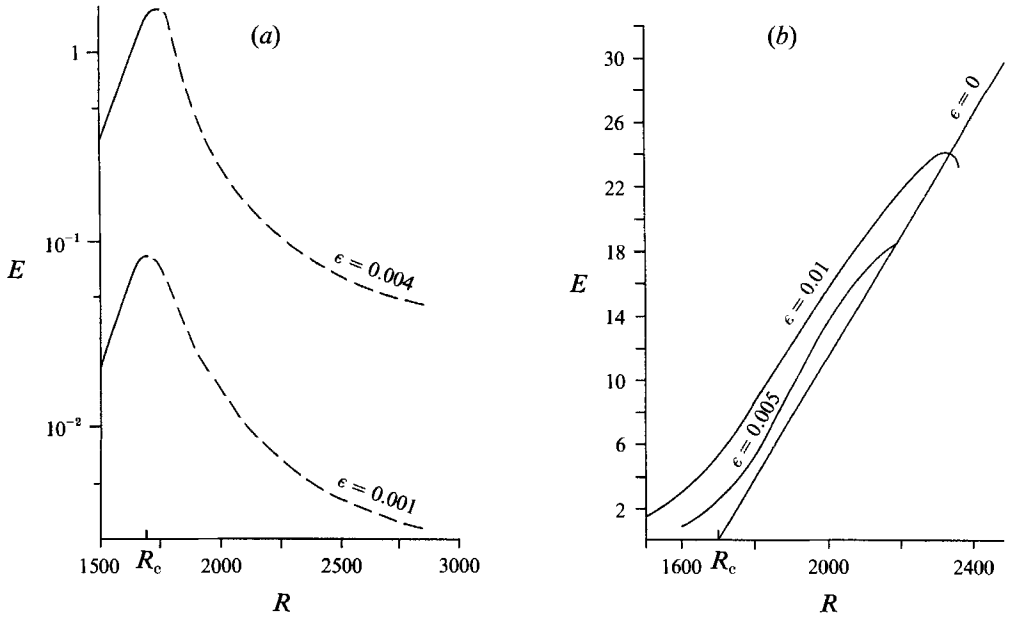

FIGURE 2. As figure 1(*a*) but for $T = 10^4$ and $\Theta_s(4,4)$: (*a*) for $\epsilon = 0.001$, 0.004 and (*b*) for $\epsilon = 0$, 0.005, 0.01, where the $\epsilon = 0$ solution corresponds to travelling waves.

at $T = 10^4$ where the critical wavenumber for the onset of convection is $m_c = 4$, and the kinetic energy E of convection is plotted as a function of the Rayleigh number R. The curve for $\epsilon = 0$ is from the solution of the corresponding uniform boundary problem. When $\epsilon \leqslant 0.004$, the effects of the non-uniform boundary respond to the spatial resonance phenomenon; when $\epsilon \geqslant 0.005$, however, the resonant effects are so large that the resonant Rayleigh number R_r is markedly different from R_c. Though the convection is largely driven by the convective instability, the boundary anomalies prevent it from forming the travelling-wave type flow. It is of importance to note that there exists a critical value $\epsilon_c \approx 0.004$. When $\epsilon_0 \leqslant 0.004$, a smooth curve $E = E(R, \epsilon = \epsilon_0)$ for the forced convection can be obtained as a function of the Rayleigh number (figure 2*a*); when $\epsilon_0 > 0.004$, *the solution curve* $E = E(R, \epsilon = \epsilon_0)$ has a turning point (figure 2*b*), to which another new branch with different character is likely to be connected. Numerically, it becomes increasingly difficult to extend the curve, due largely to the unknown character of the new branch; physically, the new branch with a smaller amplitude is likely to be unstable and therefore much less interesting. At this point in the discussion, it is much more profitable to look at the similar structure of the steady solution of the amplitude equation in the Appendix, where, the critical value ϵ_c being about $\sqrt{1.55}$, different branches of the steady solution can be obtained analytically and the corresponding curves (with or without a turning point) are presented in figure 10(*b*).

3.2. *Harmonic-resonance convection*

An important question, particularly in a rotating spherical system, is whether and how a large-scale feature of the boundary anomalies can be reflected in nonlinear convective flows when a smaller scale is dynamically preferred by the system. This is investigated by imposing a temperature imperfection

$$\Theta_s(3,3) = (1+\mathrm{i})\, Y_3^3(\theta, \phi) + \text{c.c.} \tag{18}$$

on the boundary for $T = 10^5$, where the most unstable wavenumber is $m_c = 6$. The most remarkable phenomenon observed for this case is secondary spatial resonance,

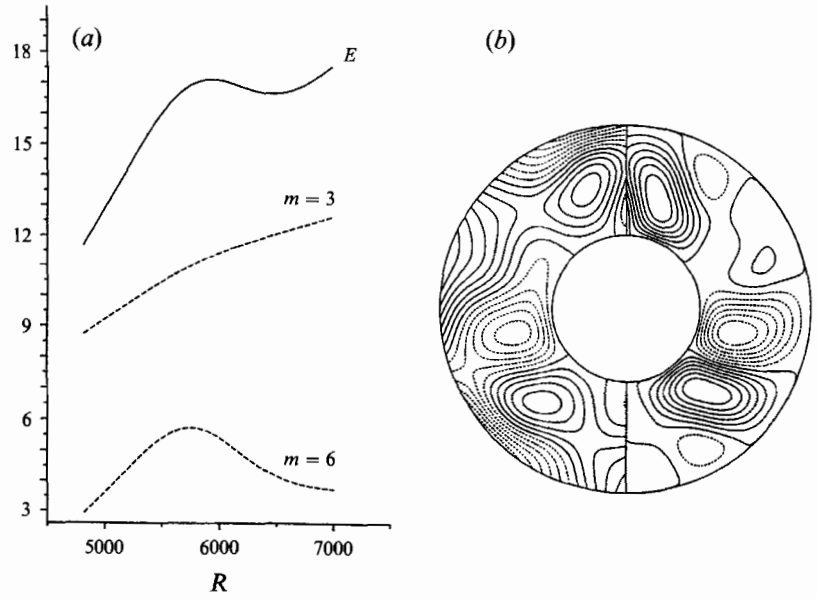

FIGURE 3. (*a*) Kinetic energies of various components of secondary resonance convection as a function of the Rayleigh number for $\epsilon = 0.08$ and $\Theta_s(3,3)$ at $T = 10^5$, (*b*) the corresponding structure for $R = 5800$.

an example of which is illustrated in figure 3(*a*). $R_c(m = 3)$ is much higher than $R_c(m = 6)$ at $T = 10^5$, and for the range $R \ll R_c(m = 3)$ the spatial resonance is a consequence of the finite-amplitude $m = 6$ mode which is produced by nonlinear interactions of the $m = 3$ mode. While the kinetic energy pertaining to the $m = 3$ mode increases nearly continuously with increasing Rayleigh number, the $m = 6$ mode gives rise to a resonance peak. We therefore call this 'harmonic resonance' convection. Because the harmonic resonance is associated with nonlinear interactions of the harmonics of the external forcing, the resonance at $m = 6$ can also occur with

$$\Theta_s(2,2) = (1+\mathrm{i})\, Y_2^2(\theta,\phi) + \mathrm{c.c.}$$

but is likely to be weaker. Similar phenomena have been discussed in other systems (Hall & Walton 1978; Pal & Kelly 1978; Coullet & Repaux 1987). The Rayleigh number R_r at which harmonic resonance occurs is again dependent on the amplitude of convection. The larger ϵ is, the higher R_r seems to be. The corresponding structure of the steady convection is shown in figure 3(*b*). It is clearly dominated by the same scale as the temperature on the boundary ($m = 3$) but with a strong modulation through other wavenumbers, mainly $m = 6$.

3.3. *Antisymmetric convection*

There are two basic spatial symmetries in a rotating spherical system with equatorially symmetric boundary conditions: they are either symmetric or antisymmetric with respect to the equatorial plane (Roberts 1968); the former symmetry is preferred because of the nature of the Coriolis forces (Busse 1970). It is thus interesting to examine whether equatorially antisymmetric boundary conditions would alter the symmetry selection.

By imposing an antisymmetric temperature boundary condition such as

$$\Theta_s(5,4) = (1+\mathrm{i})\, Y_5^4(\theta,\phi) + \mathrm{c.c.} \tag{19}$$

the equatorial symmetry of the forced convection is, strictly speaking, destroyed by the

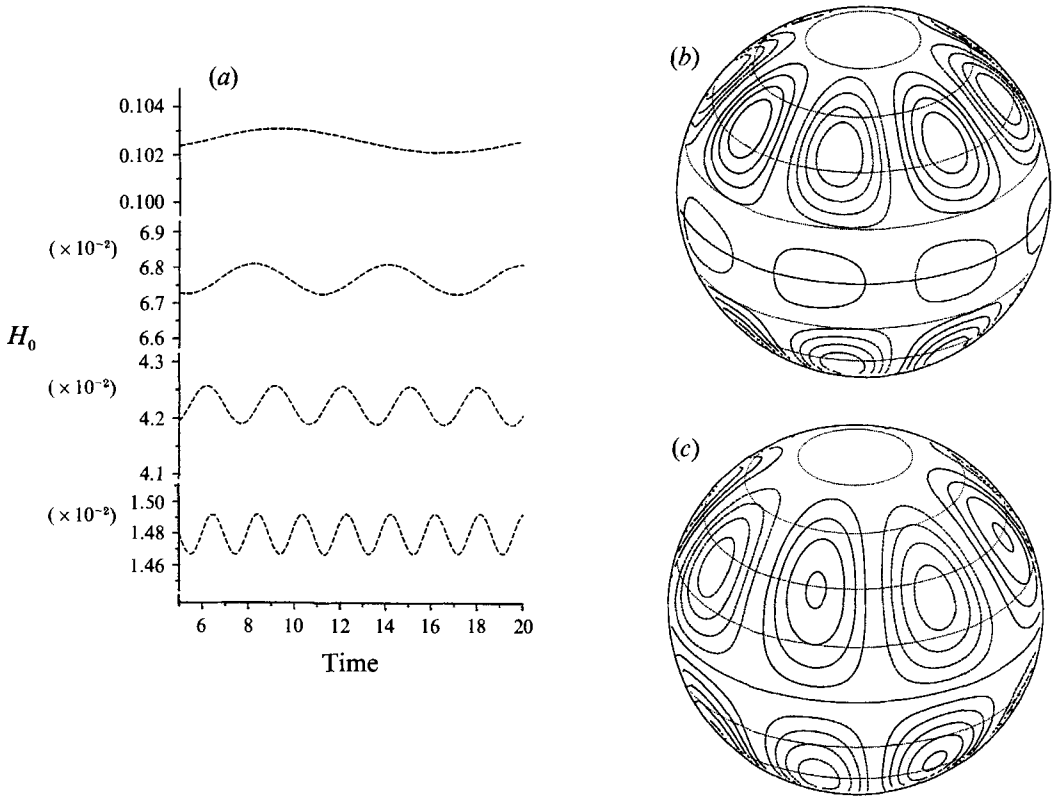

FIGURE 4. (*a*) Heat flux H_0 plotted as a function of time for different R with antisymmetric boundary conditions: reading upwards, $R = 1750, 1850, 1950, 2100$ at $T = 10^4$. (*b*) Toroidal streamlines on the outer surface of the shell for the steady solution and (*c*) time-dependent convection, both at $R = 2100$, $T = 10^4$ and $\epsilon = 0.01$.

presence of the antisymmetric boundary imperfection. However, equatorial symmetry can be still applied to individual azimuthal wavenumbers. The symmetry properties can be inferred from (7)–(9). Equations (7) and (8) are linear, the differential operators ∇^2, $\mathscr{L}$ are symmetric (that is, the symmetry properties of a field will not be changed after the operation), and the operator $\mathscr{Q}$ is antisymmetric. It follows that v has the same equatorial symmetry as that of Θ but opposite to that of w. The nonlinear term $\boldsymbol{u}\cdot\nabla(\Theta+\Theta_s)$ in (9) determines the symmetry selection of individual wavenumbers. In general, the symmetry properties of a primary solution with the boundary condition $\Theta_s(l = m_s+1, m = m_s)$ can be expressed by the following selection rules:

$$\Theta_{l,m}, v_{l,m}, w_{l+1,m}, l+m = \text{even}, \quad m = 2jm_s, \quad j = 0, 1, 2, 3, \ldots,$$
$$\Theta_{l,m}, v_{l,m}, w_{l+1,m}, l+m = \text{odd}, \quad m = (2j-1)m_s, \quad j = 1, 2, 3, \ldots,$$

where $\Theta_{l,m}$, $v_{l,m}$ and $w_{l,m}$ are the coefficients of spherical harmonics $Y_l^m(\theta, \phi)$ used for different variables. This result can also be obtained geometrically by considering rotations about the polar axis and reflexion in the equatorial plane (Gubbins & Zhang 1993). With the above symmetry properties, the amount of computation for the forced solution can be dramatically reduced.

Such convection has been examined in detail with the antisymmetric temperature boundary $\Theta_s(5, 4)$ for $T = 10^4$, where the R_c for the antisymmetric mode is about twice as large as that for the symmetric mode (Z1, figure 1). Figure 4(*b*) illustrates a typical pattern of toroidal streamlines on the outer spherical surface. The flow is clearly

dominated by the $m = 4$ mode and is largely antisymmetric with respect to the equator; the critical convection mode of the uniform boundary problem has been excluded in the forced solution by symmetry considerations, but will be included in the stability analysis of the primary solutions in §4.3.

4. Stability of the forced convection

4.1. *Stability of the boundary-resonance solution*

The conditions under which boundary-locked steady convection can survive with increasing strength of the convective instability is of crucial importance in understanding thermal coupling. Stability analysis is therefore a central element of our whole analysis, and our attention is focused on the (R, ϵ) parameter space for each case discussed in the last section. It is worth emphasizing the difference between our instability analysis and the instability analysis for the onset of convection. Only a linear analysis is required for the convective instability when $\epsilon = 0$; for the cases of $\epsilon \neq 0$, however, it is necessary to compute many nonlinear solutions in the parameter space (R, ϵ) before performing linear stability analysis on every nonlinear solution. Typically, more than 200 nonlinear solutions are obtained for each case.

The stability properties of the boundary resonance solutions for $T = 10^4$ and $\Theta_s(4,4)$ are displayed figure 5(*a*), where the instability curve of the uniform boundary problem is represented by $\epsilon = 0$. Different curves correspond to selected values of the imperfection parameter and numbers near the curves represent the characteristic frequency of the most rapidly growing disturbance. Different slopes between the curves with $\epsilon =$ constant and the curve with $\epsilon = 0$ are expected in the parameters space shown in the figure because they correspond to totally different basic states. The slopes of the curves with non-zero ϵ, however, converge to the slope of the curve with $\epsilon = 0$ when $R \ll R_c$ and the parameter ϵ is small, which are of less interest and therefore not shown in the figure. For the curves with $\epsilon > 0.004$, the zero denotes $\sigma_i = 0$ for the whole curve. The criteria of stability or instability of steady convection are based on the behaviour of a linearized system (10)–(12). A number of subsets of the linear system characterized by different Floquet parameters M were examined to determine the stability of a solution. The $M = 0$ set had the largest growth rate and therefore controls stability of the nonlinear solutions; the $M = 0$ results are shown in figure 5(*a*).

The stability analysis suggests two types of transition. In the first type, with weaker boundary effects for $\epsilon \leqslant \epsilon_c = 0.004$, the stability boundary is characterized by non-zero values of the characteristic frequency which are slightly different from the related value of the uniform boundary problem $\epsilon = 0$. The forced convection becomes unstable beyond the spatial resonance peak; the post-resonance stability region, from R_r to R_{ic}, increases significantly with increasing ϵ, as also indicated by the dashed lines in figure 1(*a*) and 2(*a*). This type of instability is likely to lead to Hopf-type bifurcation; the corresponding new solution is similar in some ways to the uniform boundary convection. In the second type, with the strong boundary effects for $\epsilon > \epsilon_c = 0.004$, the boundary-locked steady solutions become unstable at the turning point (e.g. figure 2*b*, the $\epsilon = 0.01$ curve) characterized by the zero imaginary part of eigenvalues, indicating the coalescence and disappearance of two steady solutions. One is stable and the other is unstable, with increasing the Rayleigh number, though the unstable steady branch cannot be obtained in our numerical analysis. The second type of transition is likely to be related to a saddle-node bifurcation. It strongly suggests that there exists a critical line in the parameter space (ϵ, R) lying approximately between the two points $(\epsilon, R) = [0.005, 2230]$ and $[0.03, 2500]$. Crossing this line, the stability analysis indicates

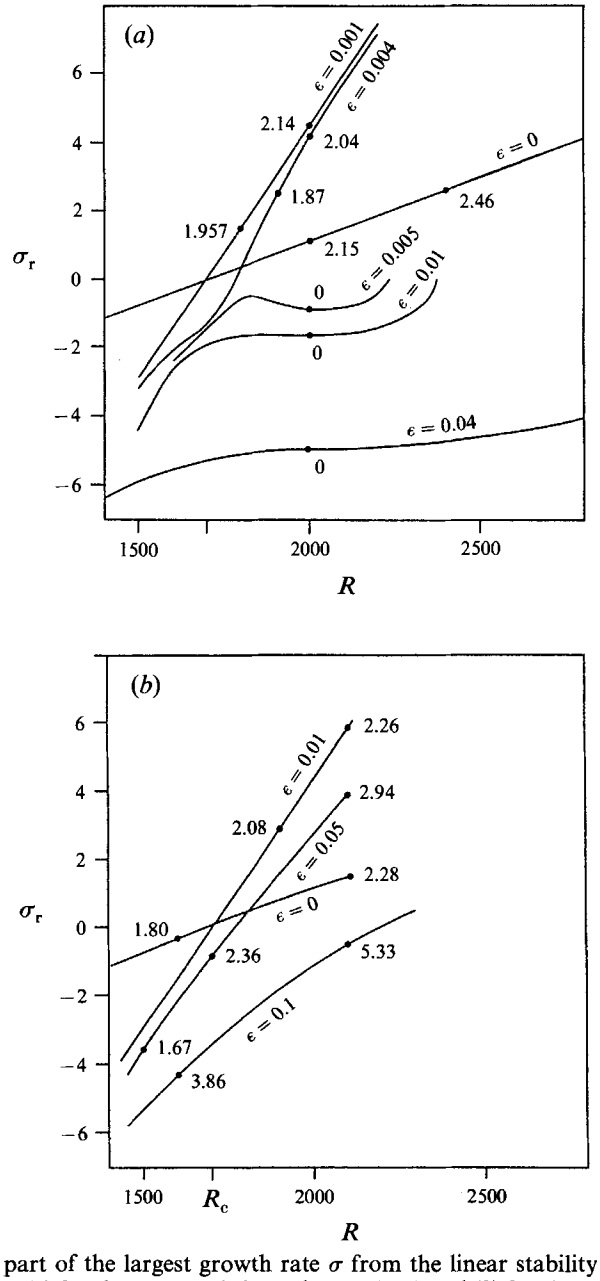

FIGURE 5. Real part of the largest growth rate σ from the linear stability analysis as a function of Rayleigh number: (*a*) for the symmetric boundary $\Theta_s(4,4)$ and (*b*) for the antisymmetric imperfection $\Theta_s(5,4)$ at $T = 10^4$.

a saddle-node bifurcation. Again it is extremely helpful to see the analogous stability analysis for the relevant amplitude equation in the Appendix, which shows almost the exactly same features of the stability properties. The precise nature of the bifurcation of course can only be revealed by obtaining the time-dependent solution of the full nonlinear convection. The remarkable feature of the saddle-node bifurcation suggested by the stability analysis will be confirmed in the next section.

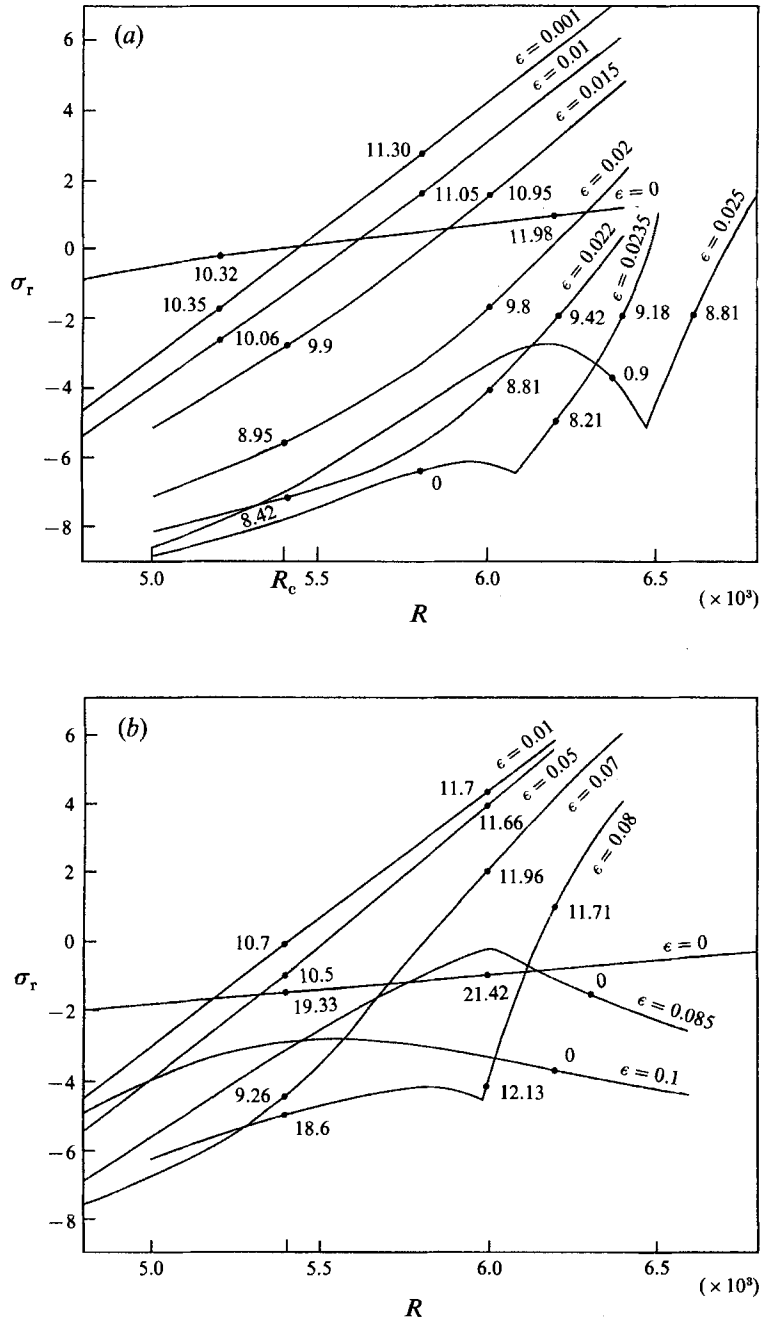

FIGURE 6. As figure 5 but for (*a*) $\Theta_s(6,6)$ and (*b*) $\Theta_s(3,3)$ at $T = 10^5$.

The appearance of the second type of transition is not only related to the strength of the boundary anomalies but also to their scale. To shed some light on this important question, the case with $T = 10^5$ and $\Theta_s(6,6)$ was also studied in detail. Its stability diagram is presented in figure 6(*a*). Not surprisingly, the boundary effects on the system become much weaker, though the system is still strongly stabilized with the

N_t	R	σ
4	5.4×10^3	$(-1.234+i10.55)$
4	5.6×10^3	$(0.205+i10.89)$
5	5.4×10^3	$(-1.230+i10.43)$
5	5.6×10^3	$(0.210+i10.76)$
6	5.4×10^3	$(-1.225+i10.39)$
6	5.6×10^3	$(0.215+i10.72)$
8	5.4×10^3	$(-1.222+i10.37)$
8	5.6×10^3	$(0.217+i10.71)$

TABLE 1. The convergence behaviour near the stability boundary with increasing truncation parameter N_t for $T = 10^5$ and $\epsilon = 0.01$

presence of the non-uniform boundary ($R_{ic} \approx 6200$ at $\epsilon = 0.02$, which is much larger than $R_c \approx 5400$ at $\epsilon = 0$). There is no indication of the saddle-node bifurcation in the parameter space studied; instead, the most unstable eigenmode switches from vanishing eigenfrequency to a different branch with non-zero values of σ_i when ϵ exceeds 0.022.

The stability boundary of a nonlinear solution is usually sensitive to the truncation. The results near the stability boundary at different levels of the truncation are shown in table 1 to give an impression of the accuracy of our analysis. Most of our results presented in this paper are calculated based on the truncation level $N_t = 6$ which appears to have a numerical inaccuracy of less than 2%.

4.2. *Stability of the harmonic-resonance solution*

A much larger value of ϵ than in the case of the resonance wavelength is needed in order to lock the convection into the boundary when a large-scale non-uniform boundary condition is imposed but a much smaller scale is selected dynamically. Displayed in figure 6(*b*) is the stability diagram or the case of $T = 10^5$ and $\Theta_s(3,3)$. Comparing figure 6(*a*) with figure 6(*b*) indicates that instability of the harmonic resonance solution is mainly caused by the convective instability in connection with the $m = 6$ mode, which has much lower R_c. As ϵ exceeds 0.08, the steady solutions dominated by the boundary wavenumber $m_s = 3$ and modulated by larger wavenumbers are locked into the boundary and stable.

Though it came as a surprise that the weak boundary modulation can change the prominent features of the convection dramatically, most of the features can be explained on the basis of two competing influences: the Rossby-wave type of convective instability and the stability of the boundary-locked flow produced by baroclinic effects. One obvious but important feature is that the non-uniform temperature boundary condition stabilizes the system. The Rayleigh number R_{ic} always exceeds the classical value of R_c. This stabilizing effect is similar to that found in Rayleigh–Bénard convection (Weber 1973).

4.3. *Stability of the antisymmetric convection*

Antisymmetric perturbations are stable for the cases of equatorially symmetric boundary conditions (Busse 1970) and can safely be ignored, but symmetric perturbations cannot be ignored in the case of equatorially antisymmetric boundary conditions. Equatorial symmetry breaking is central to the stability analysis for the forced antisymmetric convection.

Solutions of the linear homogeneous equations (10)–(12) can be divided into two

sub-classes. One of them has the same symmetry as that of the forced steady solution in §3.3, and the other is described by the following relations:

$$\Theta_{l,m}, v_{l,m}, w_{l,m}, l+m = \text{odd}, \quad m = 2jm_s, \quad j = 0, 1, 2, 3, \ldots,$$
$$\Theta_{l,m}, v_{l,m}, w_{l+1,m}, l+m = \text{even}, \quad m = (2j-1)m_s, \quad j = 1, 2, 3, \ldots,$$

which includes the critical symmetric mode for the onset of the uniform boundary convection.

The symmetric modes control the stability of the forced antisymmetric convection, and the corresponding stability diagram is shown in figure 5(*b*), where the numbers represent the imaginary part, σ_i, of the most rapidly growing perturbation. By comparing the values of σ_i from the instability analysis of the antisymmetric convection ($\epsilon > 0$ curves) with those of the most unstable mode for the perfect convection ($\epsilon = 0$ curve), it becomes clear that instabilities of the antisymmetric convection are caused by the natural mode ($m = 4$, equatorially symmetric) which is excluded in the forced antisymmetric solution. Detailed examination of the most rapidly growing eigenvector confirms this observation. For the parameter range ($R < 2R_c$) investigated in this paper, the antisymmetric temperature boundary exerts relatively much weaker influences on convection, and spatial resonance cannot occur. Even at $\epsilon = 0.05$, the instability boundary is shifted only slightly from that of the uniform boundary problem.

5. Secondary convection

5.1. *Hopf-type bifurcation*

In this case, the bifurcation is local, and linear stability analysis can usually yield useful information about the stability boundary, the physical mechanism of instability, and the form of a bifurcation solution. However, there are no grounds for determining the properties of bifurcation solutions based on linear stability analysis. With small values of ϵ shown in figures 5(*a*) and 6(*a*), the instabilities cause Hopf-type bifurcation and lead to periodic convection. Even though solutions of the nonlinear equations (13)–(15) confirm the stability boundary and oscillation frequency predicted by the instability analysis, time-dependent secondary convection shows surprisingly interesting features. An example of secondary convection for $T = 10^5$, $R = 5700$, $\epsilon = 0.01$ and $\Theta_s(6, 6)$ is displayed in figure 7; the corresponding stability curve for $\epsilon = 0.01$ is shown in figure 6(*a*). Of particular interest is the heat flux, which is negative during part of the oscillation when the kinetic energy drops to about 10% of its peak value. Detailed examination of the pattern of convection at different instants, four of which are shown in figure 7(*c*), reveals that the convection vacillates between the boundary-driven type and the boundary-resonance type. At the time of slightly negative heat transport, $t = 3.34$, the flow is concentrated near the outer boundary and is driven primarily by boundary anomalies; at the time of maximum heat transfer, $t = 3.62$, the pattern of flow resembles the resonant convection of figure 1(*d*). Also displayed in figure 7(*a*) is the solution (the solid curve) at the higher truncation $N_t = 8$ in an effort to estimate the accuracy of the secondary convection. The phase difference between the dashed ($N_t = 6$) and the solid ($N_t = 8$) curves has been offset slightly to show their small differences more clearly. In addition, there is almost no difference in convection structure for different truncation levels.

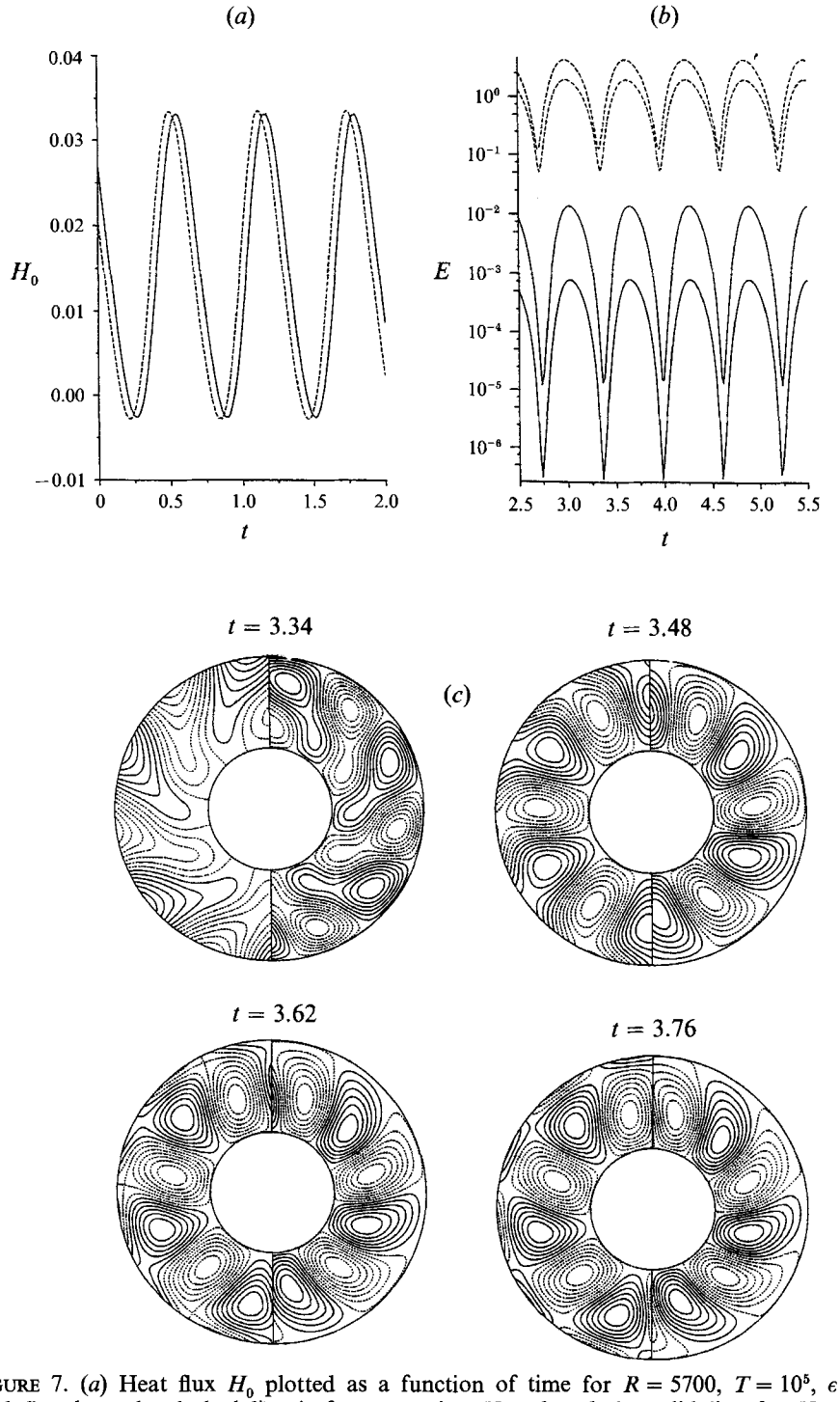

FIGURE 7. (*a*) Heat flux H_0 plotted as a function of time for $R = 5700$, $T = 10^5$, $\epsilon = 0.01$ and $\Theta_s(6, 6)$, where the dashed line is for truncation $N_t = 6$ and the solid line for $N_t = 8$. (*b*) The corresponding kinetic energies of various components. (*c*) The pattern of convection at the different instants shown.

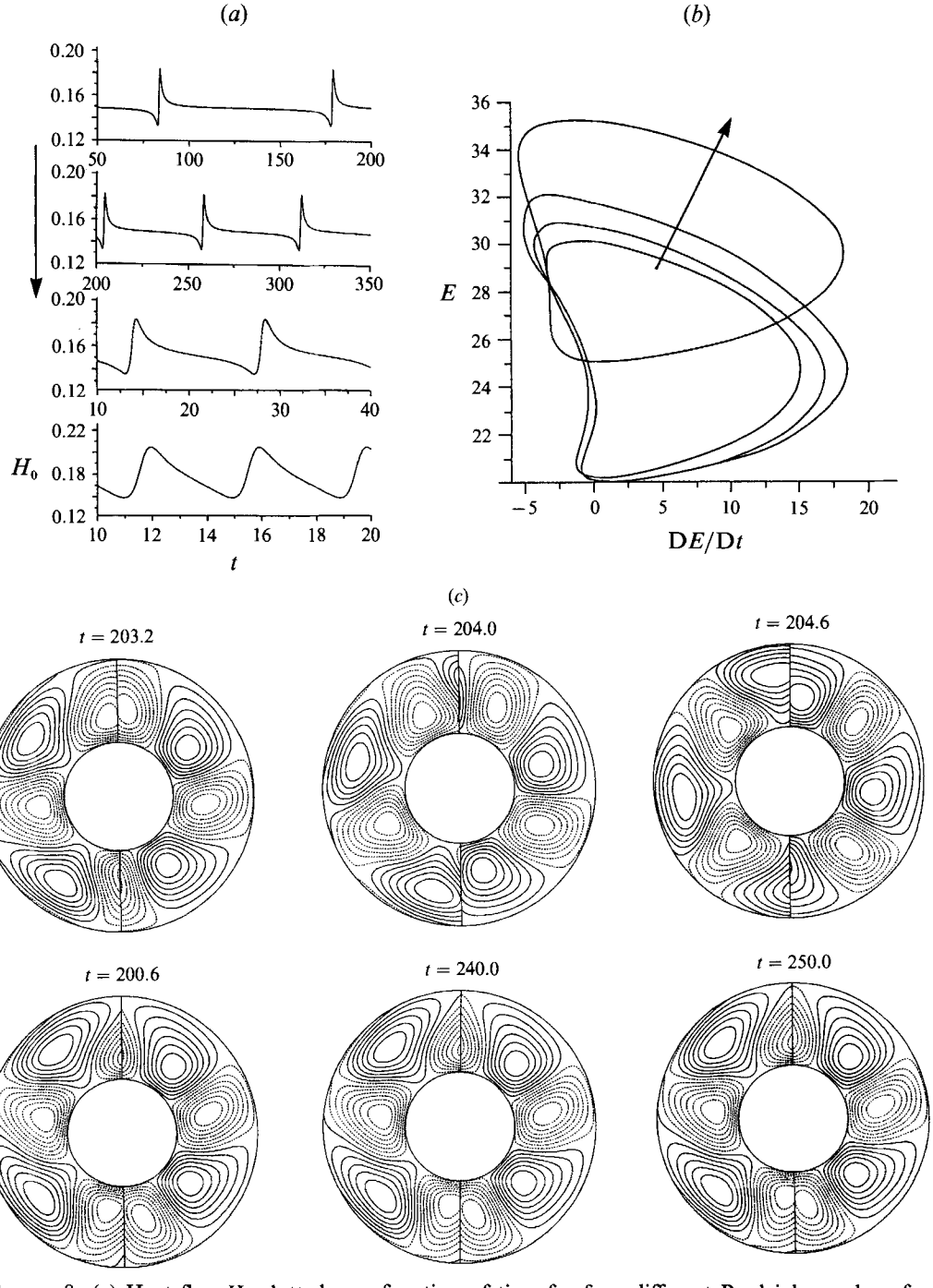

FIGURE 8. (*a*) Heat flux H_0 plotted as a function of time for four different Rayleigh numbers for (following the arrow) $R = 2369.5$, 2370, 2380, 2500 at $T = 10^4$ for $\epsilon = 0.01$ and $\Theta_s(4,4)$. (*b*) The corresponding trajectories in the phase space $(E, \dot{E})$. (*c*) The corresponding pattern of the convection at different instants for $R = 2370$.

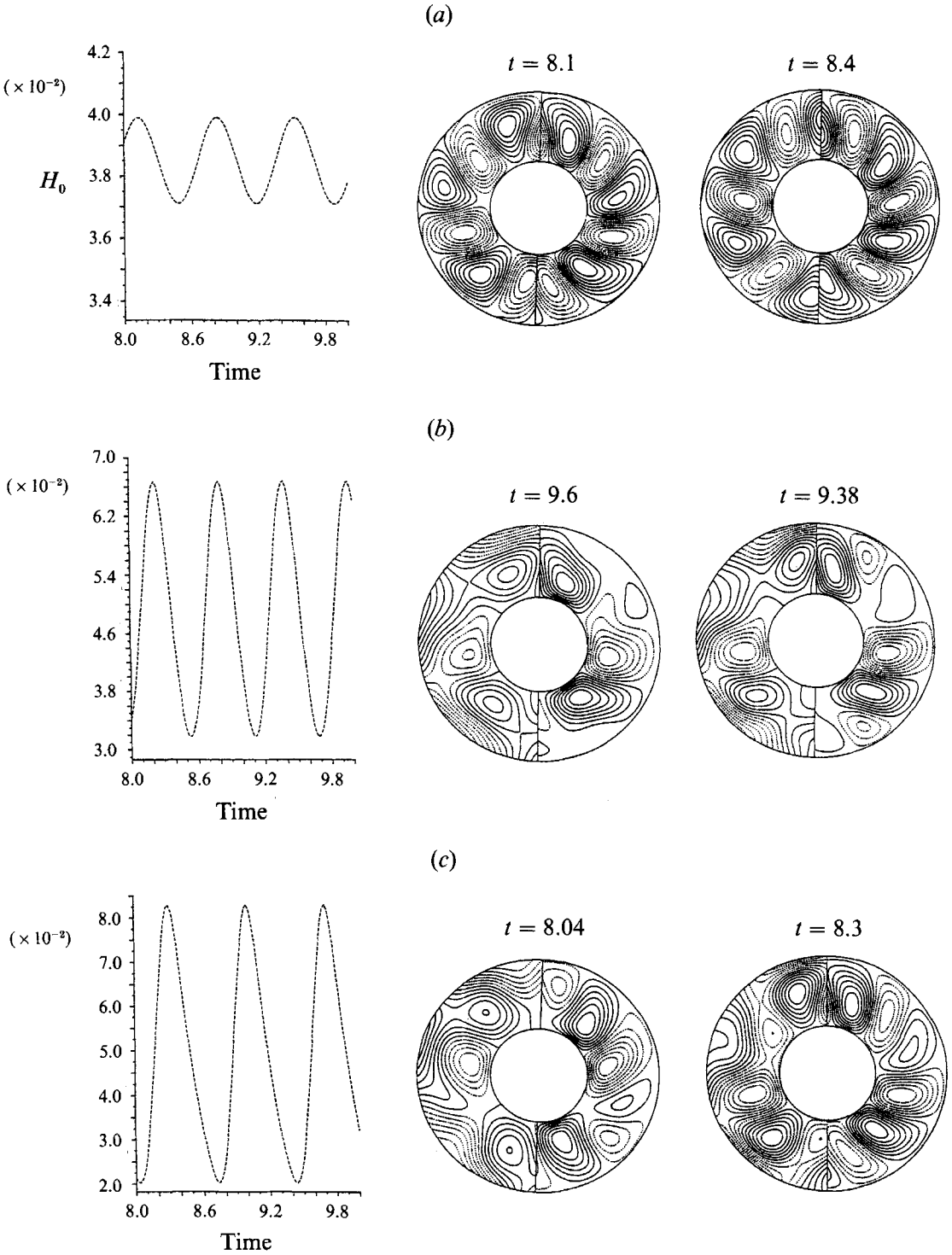

FIGURE 9. Time-dependent behaviour of the convection for $\Theta_s(3,3)$, $T = 10^5$ and $R = 5900$ with different values of ϵ: (*a*) six-roll at $\epsilon = 0.01$, (*b*) three-roll at $\epsilon = 0.07$, (*c*) vacillation between the six and three rolls at $\epsilon = 0.05$.

5.2. *Saddle-node-type bifurcation*

In this case (corresponding to the stability results in figure 5(*a*) for $T = 10^4$), the bifurcation is global and the precise nature of the secondary convection cannot be predicted based on linear stability analysis. Except possibly for the stability boundary at which the transition occurs, very little can be learnt about the behaviour of the new nonlinear convection without solving the full nonlinear problem by time integration of the system (13)–(15). When the Rayleigh number R is slightly beyond the stability boundary for $0.004 \leqslant \epsilon \leqslant 0.03$, where the imaginary part of the most rapidly growing disturbance is zero (figure 5*a*), the forced steady convection becomes unstable to oscillatory convection but the period of oscillation is extremely large. The period of oscillation decreases rapidly as $R - R_{ic}$ is increased. An example of this behaviour is illustrated in figure 8 for $\epsilon = 0.01$. The total heat flux, H_0, as a function of time for four different Rayleigh numbers is shown in figure 8(*a*), and the corresponding trajectories in the phase plane $(E, \dot{E})$ are shown in figure 8(*b*). The period of oscillation τ at $R = R_{ic} + 0.3$, where R_{ic} is about 2369.2, is $\tau \approx 100$. This decreases sharply to about $\tau \approx 12$ at $R = R_{ic} + 10.8$ while the trajectories move away from the saddle cycle. Physically, the behaviour of the nonlinear system is clear: the temperature anomalies on the boundary tend to lock the convection while the convective instability produces azimuthally travelling rolls. This physics is perhaps most clearly illuminated in the evolution of the convection pattern displayed in figure 8(*c*) at six different instants during one oscillation period. It takes a long time for the convection rolls to pass over the boundary anomalies when there is only a moderate phase difference between the rolls and the boundary temperature; the rolls move quickly when they are out of phase with the boundary temperature. Mathematically, this corresponds to a saddle-node bifurcation: two distinct steady equilibria, a sink and saddle, collide and disappear, leaving a new periodic solution in their wake. This is quite a common phenomenon in simple dynamical systems governed by an ordinary differential equation. An analogous saddle-node bifurcation for the amplitude equation is given in figure 11(*b*) in the Appendix. To the authors' knowledge, however, this is the first time that a saddle-node bifurcation has been found in a realistic convective fluid system governed by partial differential equations. Finally, it is worth noticing the similarity between figure 8(*a*) of the spherical convection and figure 11(*b*) of the amplitude equation.

5.3. *Vacillation between six and three rolls*

In a rotating spherical system, the scale of convection is determined dynamically by the Taylor number, which measures the rate of rotation, $m_c \sim T^{\frac{1}{6}}$ (Roberts 1968). For the problem of the uniform boundary convection, wavenumber-vacillation convection becomes possible in a proper parameter space (codimension-2 bifurcation) as a result of two competing scales (Z1). A non-uniformly heated boundary with a different wavelength from the critical one introduces a new competing scale; different forms of secondary convection, including the wavenumber-vacillation convection, can be obtained, in a principle, by choosing proper values of the imperfection parameter ϵ.

For $\epsilon = 0.01$ and $\Theta_s(3,3)$ at $T = 10^5$, corresponding to weak boundary effects, secondary convection (see the stability diagram figure 6*b*) is approximately described by six-roll drifting convection with a periodic change in amplitude, as shown in figure 9(*a*). The time-dependence in amplitude is caused by the different phases between drifting rolls and the temperature boundary. With larger boundary influence ($\epsilon = 0.07$, figure 9*b*), secondary convection has a dominant steady feature of three rolls, similar to the boundary-locked solution shown in figure 3(*b*), with a strong modulation from

the six-roll solution. The corresponding heat transport varies substantially during the vacillation. In an intermediate region of the parameter ϵ, the secondary convection demonstrates wavenumber vacillation between three and six rolls, as displayed in figure 9(*c*). The convection is primarily dominated by the wavenumber $m = 6$ mode ($E(m = 6) = 12.73$, $E(m = 3) = 3.78$) at the instant of maximum heat transfer $t \approx 8.30$; when heat transfer reaches a maximum ($t \approx 8.04$), the flow shows the dominant feature of three-rolls ($E(m = 6) = 2.39$, $E(m = 3) = 4.36$). The corresponding heat transport varies drastically during the vacillation.

To illustrate the bifurcation sequence with harmonic resonance convection, consider the case with heating $\Theta(3, 3)$, $T = 10^5$, $R = 5900$, and $m_c = 6$ as the imperfection parameter ϵ increases from 0 to 0.085: drifting six-roll ($\epsilon = 0$) → amplitude-vacillation six-roll ($0 < \epsilon < 0.04$) → vacillation between six and three rolls ($0.04 < \epsilon < 0.06$) → amplitude-vacillation three-roll ($0.06 < \epsilon < 0.08$) → boundary-locked steady convection ($\epsilon > 0.08$).

5.4 *Transition to nearly symmetric convection*

The effects of antisymmetric boundary conditions on convection are much less significant than those of symmetric conditions, owing largely to the strong influences of the Coriolis forces. The steady antisymmetric convection loses its stability to convection that is dominated by the symmetric mode. The secondary convection bifurcating from the forced steady antisymmetric solution, as a result of equatorial symmetry breaking, does not have any symmetries with respect to the equator. Figure 4(*a*) shows four different time-dependent solutions with increasing Rayleigh number. Just above the instability boundary at $R = 1750$, strong interactions between the two symmetries give rise to higher frequency oscillations (figure 4*a*). These interactions become increasingly insignificant with increasing Rayleigh number as the equatorial symmetric mode increasingly dominates over the antisymmetric modes, as shown by the streamlines in figure 4(*c*). When R is increased to 2100 at $\epsilon = 0.01$, there is very little difference between uniform and non-uniform boundary convection except for the weak modulation of the amplitude of convection by antisymmetric boundary anomalies.

6. Concluding remarks

We have explored the non-uniform boundary problem with special emphasis on the competing basic flows: baroclinic and convective. The former is associated with boundary temperature anomalies which tend to lock the flow into the boundary; the latter produces time-dependent convection in the form of travelling waves. Though the non-uniform boundary considered in this paper is only concerned with the temperature boundary condition, the results may provide insight into a broad range of non-uniform boundary problems because the physics of other kinds of boundary condition, such as boundary topography, is similar but much more difficult to model.

The limit of infinite Prandtl number studied in this paper represents the simplest case because advection of momentum is neglected and the non-uniform temperature boundary condition is likely to exert a maximum influence on the system. The properties of linear and nonlinear convection are quite different for fluids with different Prandtl numbers (Zhang 1992), and, thus, it is desirable to study the fluid with moderate Prandtl numbers where the momentum advection is of significance.

We thank Dr M. R. E. Proctor for valuable discussions about the problem, who also suggested the amplitude equation studied in the Appendix. Helpful discussions with Professor C. Jones in the course of revising the paper are also appreciated. K. Z. thanks

the Leverhulme Trust for a Research Fellowship. This work is supported by NERC grant GR3/8191.

Appendix. An analogous Landau equation

In parallel to our numerical analysis of the problem of rotating spherical convection, we have studied the steady solution, stability of the steady solution and the corresponding bifurcation for the analogous amplitude equation described in §1. The amplitude equation is simple but provides an important and useful mathematical framework for the understanding of our complicated nonlinear numerical solutions.

A.1. *Steady solution*

Without loss of generality, we may rewrite the amplitude equation for setting $\omega = 1$,

$$\dot{A} = (\mu + \mathrm{i})\, A - A|A|^2 + \epsilon,$$

where $|A|$ is a complex variable, ϵ is a positive imperfection parameter and μ is a positive control parameter. For a steady equilibrium solution A_0, by setting $\dot{A}_0 = 0$ and denoting $A_0 = X_0 + \mathrm{i} Y_0$ and $Z = |A_0|^2 = X_0^2 + Y_0^2$, it can be shown that Z satisfies the following cubic equation:

$$Z^3 - 2\mu Z^2 + Z(\mu^2 + 1) - \epsilon^2 = 0,$$

which can be solved analytically using a standard formula for a cubic equation. It is, however, of importance to note that the nature of bifurcation from equilibrium is closely associated with the number of real roots of this cubic equation. With one steady solution, we may expect a smooth curve $Z = Z(\mu, \epsilon = \epsilon_0)$ and the corresponding bifurcation may be local (like Hopf type); with three solutions, we expect the appearance of a turning point in the curve $Z = Z(\mu, \epsilon = \epsilon_0)$ and the corresponding bifurcation may be global (like saddle-node type). In the parameter space (μ, ϵ), regions having one and three real solutions are separated by the parameter boundaries defined by the equation

$$36 + 72\mu^2 + 36\mu^4 - 324\mu\epsilon^2 - 36\epsilon^2\mu^3 + 243\epsilon^4 = 0.$$

This equation gives rise to the two lines (figure 10*a*) in the parameter space (μ, ϵ^2) which are connected at a point ($\mu = 1.74$, $\epsilon^2 = 1.55$) and form an angle facing the direction of increasing μ and ϵ. Inside the angle (region II), there exist three real solutions; outside the angle (region I and III), there is only one solution. It follows that, for a small imperfection parameter $\epsilon^2 < 1.55$, only one steady solution Z can be found for any given value of μ. An example of the steady solution $Z = Z(\mu, \epsilon = 1)$ is presented in figure 10(*b*). Three real solutions emerge in region II with $\epsilon^2 > 1.55$. An example $Z = Z(\mu, \epsilon = 2)$ is also displayed in figure 10(*b*): there are three distinct steady solutions in the parameter range $2.72 < \mu < 4.07$ and but only one solution when $R < 2.72$ or $R > 4.07$.

A.2. *Stability of the steady solution*

To investigate the stability of the steady solution, we linearize the nonlinear equation by assuming

$$A = (X_0 + x) + \mathrm{i}(Y_0 + y),$$

where x and y are small perturbations of X_0 and Y_0. Stability of the nonlinear equilibrium is then related to the following linear equation:

$$\dot{x} = (\mu - 3X_0^2 - Y_0^2)\, x - (1 + 2X_0\, Y_0)\, y,$$
$$\dot{y} = (1 - 2X_0\, Y_0)\, x + (\mu - 3Y_0^2 - X_0^2)\, y.$$

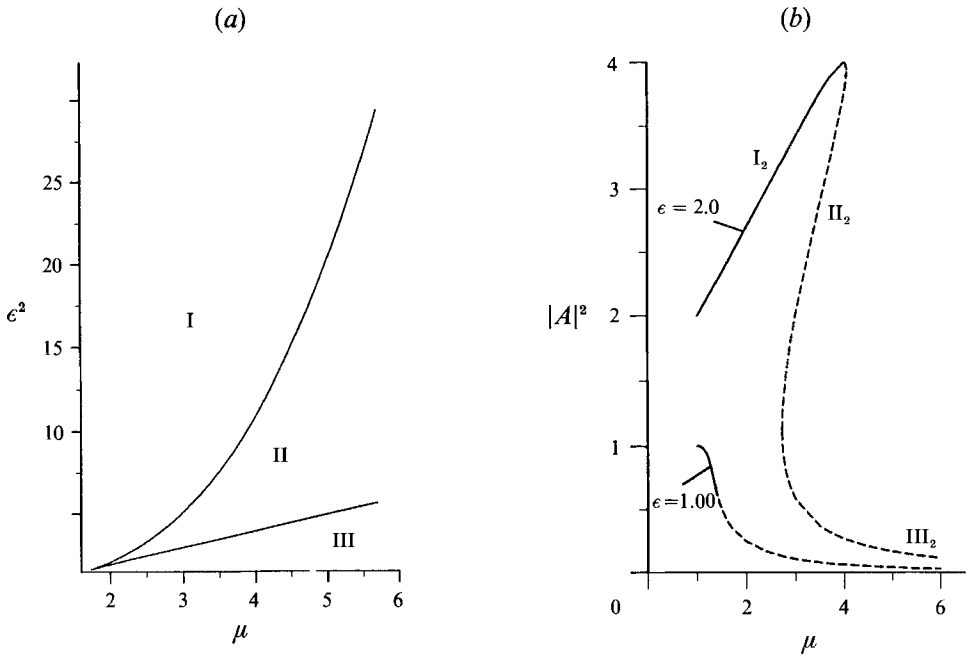

FIGURE 10. (*a*) Different regions in the parameter space (μ, ϵ^2). In regions I and III, there exits only one steady solution: in region II there exit three steady solutions. (*b*) Steady solutions $Z = Z(\mu)$ for $\epsilon = 1.0$ and 2.0.

Though the steady solution $|A_0|^2$ is algebraically complicated, the stability equation seems quite simple, the corresponding growth rate σ being given by

$$\sigma = (\mu - 2|A_0|^2) \pm (|A_0|^4 - 1)^{\frac{1}{2}}.$$

Two important features are evident from the above equation: (i) a Hopf bifurcation cannot occur if the amplitude $|A_0| > 1$; (ii) a necessary condition for the occurrence of a Hopf bifurcation is $\epsilon < \sqrt{2}$.

We again look at the examples for $\epsilon = 1.0$ and 2.0, the stability results of which are displayed in figure 10(*b*), where the dashed lines denote unstable steady solutions and the solid lines represent stable equilibria. For the smaller value $\epsilon = 1.0$, the steady solutions become unstable at $\mu_c = 1.365$. A simple pair of pure imaginary eigenvalues ($\sigma = \pm i0.731$) at the critical point indicates a Hopf bifurcation. For the larger value $\epsilon = 2$, the stability properties are more complicated because of the coexistence of the three equilibria. The steady solutions denoted by the solid line I_2 are stable (sinks) while the second branch II_2 connected with I_2 corresponds to unstable solutions (saddles). The third branch II_3 with the smallest amplitude is always the most unstable and characterized by a complex eigenvalue with a positive real part. Crossing from region II into region III in figure 10(*a*) or increasing μ from $\mu < 4.064$ to $\mu > 4.064$ at the turning point (figure 10*b*, $\epsilon = 2$), the two steady equilibria, a sink and a saddle, coalescence and subsequently disappear, suggesting a saddle-node bifurcation.

A.3. *Hopf and saddle-node bifurcation*

Both the Hopf and saddle-node bifurcations give rise to a new periodic solution. The Hopf bifurcation for small ϵ is local and, subsequently, the main features of the new periodic solution close to the critical point can be predicted on the basis of linear stability analysis, which is not true for a global saddle-node bifurcation.

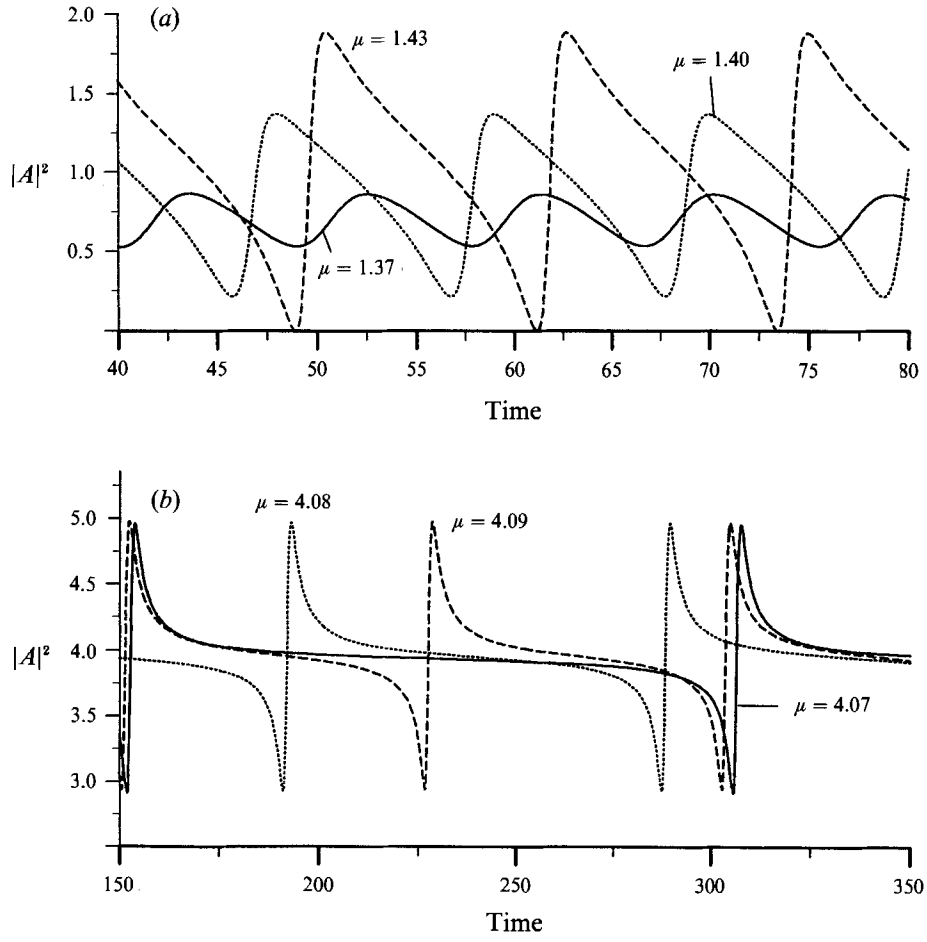

FIGURE 11. (*a*) Periodic Hopf-bifurcation solutions $|A(t)|^2$ at $\epsilon = 1.0$ and (*b*) saddle-node bifurcation solutions at $\epsilon = 2.0$ for different values of μ.

To gain an impression of new bifurcation solutions, we solve numerically the following nonlinear differential equations:

$$\dot{X} = \mu X - Y - X(X^2 + Y^2) + \epsilon,$$
$$\dot{Y} = \mu Y + X - Y(X^2 + Y^2),$$

in the neighbourhood of the bifurcation point for $\epsilon = 1.0$ and 2.0, $A(t)$ being $X(t) + \mathrm{i}Y(t)$. Figure 11 (*a*) shows three periodic solutions, $|A|^2$, as a function of time, for $\mu = 1.37$, 1.40 and 1.43 at $\epsilon = 1$, the bifurcation point being $\mu_c = 1.365$. The purely imaginary eigenvalues $\sigma = \pm \mathrm{i}0.731$ at the critical point suggest the period of the oscillation $T_0 = 8.6$ for a new nonlinear solution, while the periodic solution at $\mu = 1.370$ (the solid curve in figure 11 *a*) gives $T_0 = 8.8$. With increasing μ, the period increases from $T_0 = 11.0$ at $\mu_c = 1.40$ (the dotted curve) to $T_0 = 12.4$ at $\mu_c = 1.43$ (the dashed curve), due to the nonlinear effects of a much larger amplitude. In this case, a limit cycle emerges from the unstable equilibrium, and the behaviour of the bifurcation solution is predicted by linear analysis at the critical point. The saddle-node bifurcation is complicated but much more interesting. We present three new periodic solutions in figure 11 (*b*) for $\mu = 4.07$, 4.08 and 4.09 at $\epsilon = 2$, the bifurcation point being $\mu_c = 4.06$.

Just after the bifurcation at $\mu = 4.07$, the new solution (the solid curve in the figure) is characterized by a long period with $T_0 = 154$. The amplitude $|A|^2$ remains almost constant except in a very short interval in which $|A|^2$ reaches its peak. The period decreases rapidly, from $T_0 = 154$ to 76, when the system slightly departs from the saddle node where the coalescence of a sink and a saddle takes place.

REFERENCES

BLOXHAM, J. & GUBBINS, D. 1985 The secular variation of the earth's magnetic field. *Nature* **317**, 777–781.

BUSSE, F. H. 1970 Thermal instabilities in rapidly rotating systems. *J. Fluid Mech.* **44**, 441–460.

BUSSE, F. H. 1983 A model of mean flows in the major planets. *Geophys. Astrophys. Fluid Dyn.* **23**, 152–174.

CHANDRASEKHAR, S. 1961 *Hydrodynamic and Hydromagnetic Stability*. Clarendon.

COULLET, P. & REPAUX, D. 1987 Strong resonances of periodic patterns. *Europhys. Lett.* **3**, 573–579.

COULLET, P., REPAUX, D. & VANEL, J. M. 1986 Quasiperiodic patterns. *Contem. Maths* **56**, 19–29.

GUBBINS, D. & BLOXHAM, J. 1987 Morphology of the geomagnetic field and implications for the geodynamo. *Nature* **325**, 509–511.

GUBBINS, D. & RICHARDS, M. 1986 Coupling of the core dynamo and mantle: thermal or topographic? *Geophys. Res. Lett.* **13**, 1521–1524.

GUBBINS, D. & ZHANG, K. 1993 Symmetry properties of the dynamo equations for palaeomagnetism and geomagnetism. *Phys. Earth Planet. Inter.* **75**, 225–241.

HALL, P. & WALTON, I. 1978 The smooth transition to a convective regime in a two-dimensional box. *Phil. Trans. R. Soc. Lond.* A **358**, 199–221.

HIDE, R. 1967 Motions of the earth's core and mantle, and variations of the main geomagnetic field. *Science* **157**, 55–56.

KELLY, R. E. & PAL, D. 1976 Thermal convection induced between non-uniformly heated horizontal surfaces. *Proc. 1976 Heat Transfer and Fluid Mech. Inst.*, pp. 1–17. Stanford University Press.

KELLY, R. E. & PAL, D. 1978 Thermal convection with spatially periodic boundary conditions: resonant wavelength excitation. *J. Fluid Mech.* **86**, 433–456.

PAL, D. & KELLY, R. E. 1978 Thermal convection with spatially periodic nonuniform heatings: nonresonant wavelength excitation. *Proc. 6th Intl Heat Transfer Conf. Toronto*, pp. 181–200.

ROBERTS, P. H. 1968 On the thermal instability of a self-gravitating fluid sphere containing heat sources. *Phil. Trans. R. Soc. Lond.* A **263**, 93–117.

WEBER, J. 1973 On thermal convection between non-uniformly heated planes. *J. Heat Mass Transfer* **16**, 961–970.

YOO, J. S. & KLM, M. U. 1991 Two-dimensional convection in a horizontal fluid layer with spatially periodic boundary conditions. *Fluid Dyn. Res.* **7**, 181–200.

ZHANG, K. 1991 Vacillatory convection in a rotating spherical fluid shell at infinite Prandtl numbers. *J. Fluid Mech.* **228**, 607–628 (referred to herein as Z1).

ZHANG, K. 1992 Spiralling columnar convection in rapidly rotating spherical fluid shells. *J. Fluid Mech.* **236**, 535–556.

ZHANG, K. & BUSSE, F. 1990 Generation of magnetic fields by convection in a rotating spherical fluid shell of infinite Prandtl number. *Phys. Earth Planet. Inter.* **59**, 208–222.

ZHANG, K. & GUBBINS, D. 1992 On convection in the Earth's core forced by lateral temperature variations in the lower mantle. *Geophys. J. Intl* **108**, 247–255.